# Resonantly forced gravity–capillary lumps on deep water. Part 2. Theoretical model

## YEUNWOO CHO[1], JAMES D. DIORIO[2], T. R. AKYLAS[1]† AND JAMES H. DUNCAN[2]

[1]Department of Mechanical Engineering, Massachusetts Institute of Technology, Cambridge, MA 02139, USA

[2]Department of Mechanical Engineering, University of Maryland, College Park, MD 20740, USA

A theoretical model is presented for the generation of waves by a localized pressure distribution moving on the surface of deep water with speed near the minimum gravity–capillary phase speed, $c_{min}$. The model employs a simple forced–damped nonlinear dispersive equation. Even though it is not formally derived from the full governing equations, the proposed model equation combines the main effects controlling the response and captures the salient features of the experimental results reported in Diorio *et al.* (*J. Fluid Mech.,* vol. 672, 2011, pp. 268–287 – Part 1 of this work). Specifically, as the speed of the pressure disturbance is increased towards $c_{min}$, three distinct responses arise: state I is confined beneath the applied pressure and corresponds to the linear subcritical steady solution; state II is steady, too, but features a steep gravity–capillary lump downstream of the pressure source; and state III is time-periodic, involving continuous shedding of lumps downstream. The transitions from states I to II and from states II to III, observed experimentally, are associated with certain limit points in the steady-state response diagram computed via numerical continuation. Moreover, within the speed range that state II is reached, the maximum response amplitude turns out to be virtually independent of the strength of the pressure disturbance, in agreement with the experiment. The proposed model equation, while *ad hoc*, brings out the delicate interplay between dispersive, nonlinear and viscous effects that takes place near $c_{min}$, and may also prove useful in other physical settings where a phase-speed minimum at non-zero wavenumber occurs.

**Key words:** bifurcation, solitary waves

## 1. Introduction

This is the second part of a combined experimental and theoretical investigation of the wave pattern induced by a localized pressure source moving on the surface of deep water at speeds close to the minimum gravity–capillary phase speed, $c_{min}$. Previous related work on this problem and the motivation for the present study are discussed in detail in §1 of Diorio *et al.* (2011, hereafter referred to as Part 1). We recall that, according to linear potential-flow theory, $c_{min}$ is a resonant speed at which the forced response grows unbounded in time, suggesting that nonlinear and viscous effects would probably become important near this critical condition.

† Email address for correspondence: trakylas@mit.edu

Moreover, ignoring viscous damping, $c_{min}$ is the bifurcation point of fully localized solitary waves or lumps, which may also play a significant role in the resonant forced response. Apart from gravity–capillary water waves, these issues bear, in general, on wave systems that feature a phase-speed minimum at non-zero wavenumber.

In Part 1, we have reported on laboratory experiments conducted in a tank using as excitation a circular pressure distribution, created by blowing air onto the water surface through a small-diameter tube. Part 2 is concerned with an approximate theoretical model that is used to explain the observed responses near critical conditions.

According to the experimental observations, the wave response to a localized pressure source moving with speed near $c_{min}$ is controlled by dispersive, nonlinear, three-dimensional and transient effects; also, given that the waves of interest are in the gravity–capillary range, viscous dissipation is expected to play an important part. Moreover, as the response features steep lumps, which do not resemble modulated wavepackets as would be the case in the weakly nonlinear limit (Kim & Akylas 2005), nonlinearity cannot be assumed weak.

Rather than the full unsteady, nonlinear, viscous water-wave problem in three dimensions, the ensuing analysis is based on a simple model equation. Even though it is not obtained from the exact governing equations via a systematic approximation procedure, this equation combines the main effects controlling the response and captures the essential features of the observations. Furthermore, the proposed model adds to the physical understanding of the response by bringing out the delicate interplay between dispersive, nonlinear and viscous effects that takes place near $c_{min}$. A similar *ad hoc* approach is taken in Whitham (1974, §13.14) in an attempt to shed light on water-wave breaking, a phenomenon also not amenable to weakly nonlinear treatment.

The model equation analysed in the present paper was also employed for the numerical simulations of transient responses presented in Diorio *et al.* (2009). In this earlier, preliminary study, viscous dissipation was assumed to act precisely as in linear waves, and results from numerical simulations were compared with experimental observations for a single excitation amplitude. Near critical conditions, three distinct responses, state I, II and III, were identified, in qualitative agreement with the experiment. However, state II, which experimentally was found to be steady, turned out to be time-periodic according to the model. Here, a systematic study of the effects of damping and forcing on steady-state and transient responses is made, and the cause of the discrepancy between the theoretical model and the experiment, noted in Diorio *et al.* (2009), is elucidated.

## 2. Model formulation

We now present the various terms in the model equation. The starting point is the dispersion relation of the potential-flow theory for linear sinusoidal gravity–capillary waves of frequency $\omega$ and wavenumber $k$ on deep water,

$$\omega^2 = \tfrac{1}{2}k(1 + k^2), \tag{2.1}$$

written in dimensionless form, normalizing to 1 the minimum of the phase speed, $c(k) = \omega/k$, and the corresponding wavenumber $k_{min}$. On kinematic grounds, at steady state, a locally confined source moving with dimensionless speed $\alpha$ would excite waves that satisfy

$$\alpha \cos\phi = c(|\boldsymbol{k}|), \tag{2.2}$$

here $\phi$ being the inclination of the wavevector $\boldsymbol{k}$ to the line of motion of the source (Whitham 1974, §12.4). Hence, the phase speed of all these wave components must be less than or equal to $\alpha$. In the case of interest, where the source speed is close to the minimum phase speed, $\alpha \approx 1$, the kinematic constraint (2.2) requires that $|\boldsymbol{k}| \approx 1$ and $\phi \ll 1$. Accordingly, a forcing moving along $x$, say, with near-critical speed would generate waves with $\boldsymbol{k} = (k, l)$ close to $\boldsymbol{k}_{min} = (\pm 1, 0)$. This suggests approximating the dispersion relation (2.1) in the neighbourhood of the phase speed minimum; for a left-going source as in the experiment, in particular, expanding (2.1) to second order around $\boldsymbol{k}_{min}$ yields

$$\omega = -\tfrac{1}{4}\,\mathrm{sgn}(k)(1 + 2\,|k| + k^2 + 2l^2). \tag{2.3}$$

To account for viscous dissipation, we shall modify (2.3) by adding an imaginary part representing the wave decay rate due to viscous damping:

$$\omega = -\mathrm{i}\tilde{\nu}\,|\boldsymbol{k}|^2 - \tfrac{1}{4}\,\mathrm{sgn}(k)(1 + 2\,|k| + k^2 + 2l^2), \tag{2.4}$$

where $\tilde{\nu}$ is a constant. This choice is consistent with the classic result obtained by Lamb (1993, §348–349) for the viscous decay rate of linear sinusoidal waves, where $\tilde{\nu}$ turns out to be equal to $\tilde{\nu}_0 = \nu(4g)^{1/4}(\rho/\tau)^{3/4}$, $\nu$ being the kinematic viscosity. (In cgs units, $\nu = 0.01$, $g = 981$, $\rho = 1$ and $\tau = 73$, so $\tilde{\nu}_0 = 0.003$.) More recently, Longuet-Higgins (1997) examined viscous dissipation in deep-water gravity–capillary solitary waves. The expression for the decay rate in (2.4) turns out to be also valid for small-amplitude solitary waves, which resemble modulated wavepackets (Akylas 1993; Longuet-Higgins 1993); in this instance, however, $\tilde{\nu} = 2\tilde{\nu}_0$, due to the spreading out of the wave envelope as the amplitude decreases. In the other extreme, steep depression solitary waves, owing to the sharply increased curvature in the wave troughs, experience far more rapid decay than their weakly nonlinear counterparts. Here, (2.4) will be assumed to hold in general, irrespective of the wave steepness; however, rather than taking $\tilde{\nu} = \tilde{\nu}_0$ as in Diorio *et al.* (2009), $\tilde{\nu}$ will be treated as a parameter that controls the strength of viscous damping and will be fixed later (see §4.1).

Making use of

$$\omega \leftrightarrow \mathrm{i}\frac{\partial}{\partial t}, \quad (k, l) \leftrightarrow -\mathrm{i}\left(\frac{\partial}{\partial x}, \frac{\partial}{\partial y}\right), \quad \mathrm{sgn}(k) \leftrightarrow \mathrm{i}\mathscr{H}, \tag{2.5}$$

where $\mathscr{H}\{f\} = \mathscr{F}^{-1}\{-\mathrm{i}\,\mathrm{sgn}(k)\mathscr{F}\{f\}\}$ stands for the Hilbert transform, with

$$\mathscr{F}\{f\} = \frac{1}{2\pi}\int_{-\infty}^{\infty} f(x)\,\mathrm{e}^{-\mathrm{i}kx}\,\mathrm{d}x \tag{2.6}$$

being the Fourier transform, it is straightforward to write down the linear differential equation that corresponds to (2.4) and combines dispersive effects near $c_{min}$ with viscous damping. Adding then the effect of forcing due to a pressure source $Ap(\xi, y)$ moving from right to left along $x$ with speed $\alpha$, the following forced equation for the free-surface elevation $\eta(\xi, y, t)$ is obtained:

$$\eta_t - \tilde{\nu}(\eta_{\xi\xi} + \eta_{yy}) + \left(\alpha - \tfrac{1}{2}\right)\eta_\xi - \tfrac{1}{4}\mathscr{H}\{\eta_{\xi\xi} + 2\eta_{yy} - \eta\} = Ap_\xi, \tag{2.7}$$

where $\xi = x + \alpha t$ and $A$ is a parameter that controls the peak amplitude of the applied pressure distribution.

To complete the model, it remains to account for nonlinearity. In the interest of simplicity, we add to (2.7) a quadratic nonlinear term of the Korteweg–de Vries (KdV)

type:

$$\eta_t - \tilde{\nu}(\eta_{\xi\xi} + \eta_{yy}) + (\alpha - \tfrac{1}{2})\eta_\xi - \beta(\eta^2)_\xi - \tfrac{1}{4}\mathscr{H}\{\eta_{\xi\xi} + 2\eta_{yy} - \eta\} = Ap_\xi. \tag{2.8}$$

In the absence of damping and forcing, (2.8) reduces to the model equation proposed in Akers & Milewski (2009) for freely propagating, inviscid, gravity–capillary two-dimensional solitary waves and lumps on deep water. Following Akers & Milewski (2009), the coefficient of the nonlinear term is fixed to

$$\beta = \sqrt{11/2}/8. \tag{2.9}$$

This choice ensures that, in the small-amplitude limit, free ($A = 0$), inviscid ($\tilde{\nu} = 0$) lump solutions of the model equation (2.8) agree, to leading order, with their weakly nonlinear counterparts of the full potential-flow theory of water waves (Kim & Akylas 2005).

Briefly, small-amplitude inviscid lumps are modulated wavepackets with carrier and envelope propagating at the same speed $\alpha$ slightly below the minimum phase speed ($\alpha < 1$). According to the model equation (2.8), for $\tilde{\nu} = A = 0$, these solutions can be expanded close to their bifurcation point $\alpha = 1$ as

$$\eta = \tfrac{1}{2}\epsilon\left\{S(X, Y)\,e^{i\xi} + \text{c.c.}\right\} + \tfrac{1}{2}\epsilon^2\left\{S_2(X, Y)\,e^{2i\xi} + \text{c.c.}\right\} + \cdots, \tag{2.10}$$

where $\alpha = 1 - \epsilon^2$ ($0 < \epsilon \ll 1$) and $(X, Y) = \epsilon(\xi, y)$. Substituting (2.10) into (2.8), the envelope of the primary harmonic is governed by

$$-S + \tfrac{1}{4}(S_{XX} + 2S_{YY}) + \tfrac{11}{32}S^2S^* = 0, \tag{2.11}$$

the same steady nonlinear Schrödinger (NLS) equation (after allowing for the difference in normalization) as found in Kim & Akylas (2005) for weakly nonlinear lumps on the basis of potential-flow theory.

The NLS equation (2.11) provides a link of the model equation (2.8) to the full water-wave problem only in the weakly nonlinear limit. Nonetheless, in our attempt to understand the rather steep lumps observed experimentally, we shall make use of (2.8) regardless of wave steepness. The predictions of our model, therefore, are expected to be qualitative at best. For instance, figure 1 shows plots of maximum depression against wave speed $\alpha$ of free, inviscid lumps, as obtained from numerical solutions of the model equation (2.8) for $A = \tilde{\nu} = 0$ (Akers & Milewski 2009; Cho 2010), the full potential-flow theory of water waves (E. Părău, personal communication 2010) and the leading-order weakly nonlinear approximation according to expansion (2.10). The model equation, although a definite improvement upon the weakly nonlinear theory away from the bifurcation point, overpredicts the peak amplitude of depression lumps of the exact inviscid theory. This discrepancy can be mitigated to some extent by adding to (2.7), rather than merely a quadratic term, a combination of quadratic and cubic nonlinearities, $(\beta_1\eta^2 + \beta_2\eta^3)_\xi$, choosing the coefficients $\beta_1$ and $\beta_2$ so that both the $O(\epsilon)$ and $O(\epsilon^2)$ terms in expansion (2.10) agree with the full theory (Cho 2010). However, the overall gain does not seem worth the added complication, given that the nonlinear nature of viscous damping was ignored earlier, among other crude assumptions.

## 3. Steady-state responses

Perhaps the most striking nonlinear feature of the wave response as the forcing speed approaches $c_{min}$, revealed by the experimental observations in Part 1, is the sudden jump from states I to II, which occurs at a critical speed $\alpha_c < 1$ depending on the
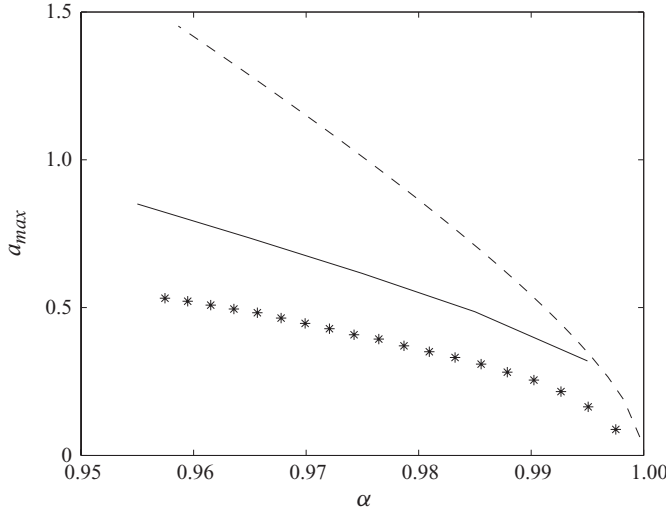
FIGURE 1. Plots of the maximum depression, $a_{max}$, against wave speed $\alpha$ of free, inviscid lumps of depression. Lines and symbols: ——, model equation (2.8) with $A = \tilde{v} = 0$; -----, leading-order weakly nonlinear approximation; ***, full potential-flow theory (E. Părău, personal communication 2010).

strength of the pressure disturbance. State I is locally confined beneath the applied pressure, similar to the subcritical response predicted by linear theory (Rayleigh's solution), whereas state II is nonlinear as it features a steep lump downstream of the excitation (see figure 4*a–d* of Part 1). In an effort to understand the transition from states I to II, we shall make a systematic study, based on the model equation (2.8), of steady-state responses as the forcing speed $\alpha$ is increased towards 1, for various values of the excitation amplitude $A$ and damping parameter $\tilde{v}$. Throughout this paper, the disturbance $p(\xi, y)$ in (2.8) will be assumed to be in the form of a Gaussian centred at $\xi = y = 0$:

$$p(\xi, y) = \exp(-2\xi^2 - 2y^2). \tag{3.1}$$

### 3.1. *Shifted lumps*

Guided by the nature of state II, we first look for possible subcritical steady-state solutions of (2.8) in the form of a finite-amplitude lump, slightly modified by forcing and damping. To this end, we write

$$\eta = \bar{\eta}(\xi - \theta, y) + \tilde{\eta}(\xi, y). \tag{3.2}$$

Here, $\bar{\eta}$ denotes a free, undamped depression-lump solution of (2.8) with speed $\alpha < 1$,

$$\left(\alpha - \tfrac{1}{2}\right)\bar{\eta}_\xi - \beta(\bar{\eta}^2)_\xi - \tfrac{1}{4}\mathscr{H}\left\{\bar{\eta}_{\xi\xi} + 2\bar{\eta}_{yy} - \bar{\eta}\right\} = 0, \tag{3.3}$$

here $\theta$ being an as-yet-undetermined constant shift of the lump profile relative to the pressure source, and $\tilde{\eta}$ is a correction term.

Inserting (3.2) into (2.8) and making use of (3.3), it is found that $\tilde{\eta}$ satisfies

$$\left(\alpha - \tfrac{1}{2}\right)\tilde{\eta}_\xi - 2\beta\left(\bar{\eta}(\xi - \theta, y)\tilde{\eta}\right)_\xi - \tfrac{1}{4}\mathscr{H}\left\{\tilde{\eta}_{\xi\xi} + 2\tilde{\eta}_{yy} - \tilde{\eta}\right\}$$
$$= \tilde{v}(\bar{\eta}_{\xi\xi} + \bar{\eta}_{yy}) + Ap_\xi + \tilde{v}(\tilde{\eta}_{\xi\xi} + \tilde{\eta}_{yy}) + \beta(\tilde{\eta}^2)_\xi. \tag{3.4}$$

Taking forcing and damping effects to be weak ($A \ll 1$, $\tilde{v} \ll 1$), we put

$$\tilde{v} = \mu A, \tag{3.5}$$

where $\mu$ is a parameter that measures the relative importance of damping, and expand the solution to (3.4) as

$$\tilde{\eta} = A\tilde{\eta}^{(1)} + A^2\tilde{\eta}^{(2)} + \cdots, \tag{3.6}$$

with a similar expansion for the shift $\theta$:

$$\theta = \theta^{(0)} + A\theta^{(1)} + \cdots. \tag{3.7}$$

The same sort of perturbation procedure has also been used in analysing finite-amplitude steady-solution branches of a forced–damped fifth-order KdV equation (Cho & Akylas 2009).

Upon substituting (3.6) into (3.4) and using (3.5) and (3.7), it is found that $\tilde{\eta}^{(1)}$ is governed by the forced equation

$$(\alpha - \tfrac{1}{2})\tilde{\eta}^{(1)}_\xi - 2\beta(\bar{\eta}(\xi - \theta^{(0)}, y)\tilde{\eta}^{(1)})_\xi - \tfrac{1}{4}\mathscr{H}\left\{\tilde{\eta}^{(1)}_{\xi\xi} + 2\tilde{\eta}^{(1)}_{yy} - \tilde{\eta}^{(1)}\right\} = R^{(1)}, \tag{3.8}$$

where

$$R^{(1)} = p_\xi + \mu(\bar{\eta}_{\xi\xi}(\xi - \theta^{(0)}, y) + \bar{\eta}_{yy}(\xi - \theta^{(0)}, y)). \tag{3.9}$$

The adjoint to the operator on the left-hand side of (3.8) is

$$\left(\alpha - \frac{1}{2}\right)\frac{\partial}{\partial\xi} - 2\beta\bar{\eta}(\xi - \theta^{(0)}, y)\frac{\partial}{\partial\xi} - \frac{1}{4}\mathscr{H}\left\{\frac{\partial^2}{\partial\xi^2} + 2\frac{\partial^2}{\partial y^2} - 1\right\}, \tag{3.10}$$

and, in view of (3.3), $\bar{\eta}(\xi - \theta^{(0)}, y)$ is a homogeneous adjoint solution that goes to zero as $\xi \to \pm\infty$, $y \to \pm\infty$. Therefore, appealing to the standard solvability argument, for the forced equation (3.8) to also have a well-behaved solution, $R^{(1)}$ must satisfy

$$\int_{-\infty}^{\infty}\int_{-\infty}^{\infty} R^{(1)}\bar{\eta}(\xi - \theta^{(0)}, y)\,\mathrm{d}\xi\,\mathrm{d}y = 0. \tag{3.11}$$

Making use of (3.9), the solvability condition (3.11) takes the form

$$\mu\int_{-\infty}^{\infty}\int_{-\infty}^{\infty}(\bar{\eta}_\xi^2 + \bar{\eta}_y^2)\,\mathrm{d}\xi\,\mathrm{d}y = -\int_{-\infty}^{\infty}\int_{-\infty}^{\infty} p(\xi, y)\bar{\eta}_\xi(\xi - \theta^{(0)}, y)\,\mathrm{d}\xi\,\mathrm{d}y. \tag{3.12}$$

This furnishes an equation for determining the shift $\theta^{(0)}$, depending on the forcing speed $\alpha$ and the parameter $\mu$.

Note that $\theta^{(0)}$ appears only on the right-hand side of (3.12), while $\mu$ solely multiplies the left side. For $\mu = 0$, in particular, since $p(\xi, y)$ is even in $\xi$ according to (3.1), $\theta^{(0)} = 0$ satisfies (3.12) regardless of $\alpha$. As expected, in the absence of damping, the proposed response (3.2) is symmetric relative to the applied pressure and tends to the free-lump solution as $\alpha$ becomes more subcritical. On the other hand, for $\mu > 0$, the solvability condition (3.12) can be satisfied for two non-zero values of $\theta^{(0)}$ when $\alpha$ exceeds a certain threshold value, $\alpha_2$, depending on $\mu$, but no solution is possible if $\alpha < \alpha_2$ (figure 2a). Accordingly, damping causes finite-amplitude steady-state solution branches to eventually turn around as $\alpha$ is decreased, and the turning point $\alpha = \alpha_2$ moves further away from $\alpha = 1$ when $\mu$ is decreased (figure 2b). Moreover, since $\mu = \tilde{v}/A$, increasing the excitation amplitude $A$ has the same effect as reducing the damping parameter $\tilde{v}$.

It is interesting that the values of $\theta^{(0)}$ for $\mu = 0.033$ displayed in figure 2(a) are positive, and this turns out to be generally the case in the range $0.01 \leqslant \mu \leqslant 0.1$ we
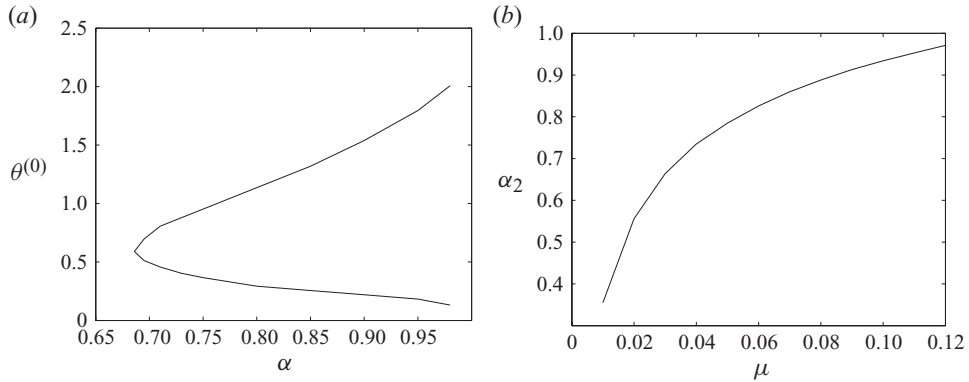
FIGURE 2. Predictions of the solvability condition (3.12) regarding the lump accompanying state II. (*a*) Downstream shift $\theta^{(0)}$ of the lump profile relative to the applied pressure versus forcing speed $\alpha$, for $\mu = 0.033$; the parameter $\mu$, defined in (3.5), measures the importance of damping relative to forcing. (*b*) Limit point $\alpha = \alpha_2$ below which shifted-lump solution is not possible, as a function of $\mu$.

examined. The lump profile in (3.2) is thus shifted in the downstream direction relative to the applied pressure, consistent with state II observed in the experiment. In fact, as discussed below, numerical continuation reveals that state II is associated with the larger of the two possible values of $\theta^{(0)}$ for $\alpha > \alpha_2$.

### 3.2. *Numerical continuation*

For highly subcritical speed $\alpha$ and small excitation amplitude $A$, the solution to the model equation (2.8) is expected to reach the linear subcritical steady state (Rayleigh's solution), which is locally confined in the vicinity of the applied pressure, similar to state I. Using numerical continuation, we shall now follow this small-amplitude steady-state solution branch as $\alpha$ is increased towards 1, for different values of $A$ and $\tilde{\nu}$, in order to make the connection with the finite-amplitude states found by perturbation theory in § 3.1.

The steady version of (2.8) was discretized using fourth-order centred finite differences, and the Hilbert transform was computed using the discrete Hilbert transform (Kak 1970). Exploiting symmetry, only $y \geqslant 0$ was considered, and the edges of the computational domain, $(\xi_{-\infty} < \xi < \xi_{+\infty}, 0 \leqslant y < y_{+\infty})$, were placed far enough so as to have negligible effect on the overall response. The resulting nonlinear equation system was solved by Newton's method, combined with pseudo-arclength continuation. The results reported here were obtained using 256 grid points along $\xi$ and 64 grid points along $y$ with $\xi_{+\infty} = -\xi_{-\infty} = y_{+\infty} = 18.85$.

We first consider the inviscid limit, $\tilde{\nu} = 0$, where the subcritical response is symmetric relative to the applied pressure. As $\alpha$ is increased, Rayleigh's solution branch turns around at a limit point before reaching $\alpha = 1$ and then follows asymptotically the finite-amplitude solution branch corresponding to free, inviscid lumps. This result is consistent with our perturbation analysis (§ 3.1) for $\mu = 0$ as well as the full potential-flow computations of Părău, Vanden-Broeck & Cooker (2005). The location of the limit point, $\alpha = \alpha_c$, is quite sensitive to the excitation amplitude $A$, $\alpha_c$ moving closer to $\alpha = 1$ as $A$ is decreased (figure 3). For the choice $A = 0.23$, in particular, it turns out that $\alpha_c = 0.92$, which matches approximately the critical speed at which transition from states I to II was observed experimentally in Part 1 for the experimental forcing amplitude $\epsilon = 0.43$ (see figure 6 of Part 1).
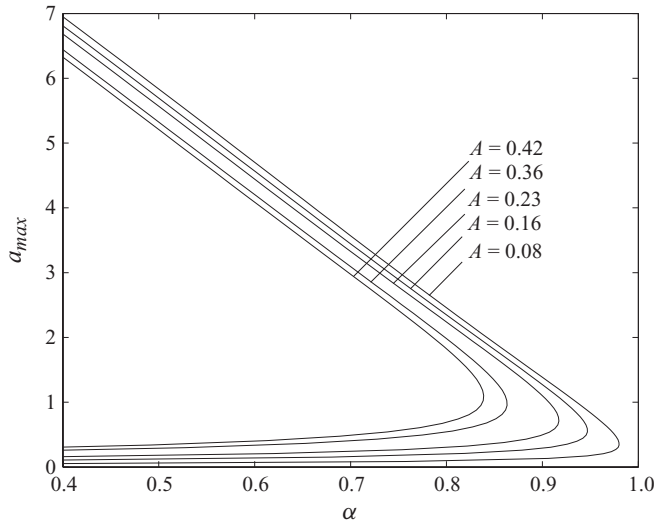
FIGURE 3. Inviscid ($\tilde{\nu} = 0$) steady-state response diagrams of the maximum depression, $a_{max}$, versus forcing speed $\alpha$ for five different excitation amplitudes $A$.

Next, we turn to the role of dissipation ($\tilde{\nu} > 0$). Figure 4 summarizes the results of numerical continuation in $\alpha$ of the small-amplitude subcritical solution branch, for $A = 0.23$ and four different values of $\tilde{\nu}$, expressed in terms of $\tilde{\nu}_0 = 0.003$, the value of $\tilde{\nu}$ pertaining to linear waves (Lamb 1993, § 348–349). For the two lower values of $\tilde{\nu} = \tilde{\nu}_0, 2\tilde{\nu}_0$ (figure 4*a,b*), dissipation has little effect until the small-amplitude solution branch turns around, and the location of the turning point remains virtually unchanged from the inviscid value, $\alpha_c = 0.92$. As $\alpha$ is decreased past $\alpha_c$, however, dissipation comes into play; as a result, the response eventually reverses course again after encountering a second turning point, $\alpha = \alpha_2$, and heads back towards $\alpha = 1$ along a neighbouring path. As the second turning point is approached, the response becomes quite steep, and the maximum depression, $a_{max}$, plotted in figure 4(*a,b*), is sensitive to small changes of the speed $\alpha$; this explains the rather complicated trajectory followed by the solution branch near the second turning point. For $\tilde{\nu} = \tilde{\nu}_0$, in fact, several turning points are found in this neighbourhood, and $\alpha_2$ is chosen as the one corresponding to the smallest speed $\alpha$ (figure 4*a*). As expected, for the larger values of $\tilde{\nu} = 6\tilde{\nu}_0, 8\tilde{\nu}_0$ (figure 4*c,d*), the increased dissipation causes the response to be less steep, and the turning points $\alpha_c$ and $\alpha_2$ are now closer to $\alpha = 1$.

The presence of a second turning point, due to dissipation, in the response diagrams shown in figure 4 confirms the predictions of the perturbation theory (figure 2), and the analytical estimates for $\alpha_2$ based on (3.12) are in reasonable agreement with the values obtained from numerical continuation (see table 1). In line with the perturbation analysis, both before and after turning around at $\alpha_2$, the numerically computed responses feature a finite-amplitude depression lump shifted downstream relative to the forcing; this shift becomes more noticeable after turning around at $\alpha_2$ and keeps increasing while the lump steepness decreases, as $\alpha$ moves further away from $\alpha_2$.

Figure 5 shows representative wave profiles at four different speeds along the response curve for $A = 0.23$ and $\tilde{\nu} = 2\tilde{\nu}_0$ (figure 4*b*). We recall that, for this value of the excitation amplitude $A$, the first turning point, $\alpha_c = 0.92$, according to the model, is close to the critical speed at which the jump from states I
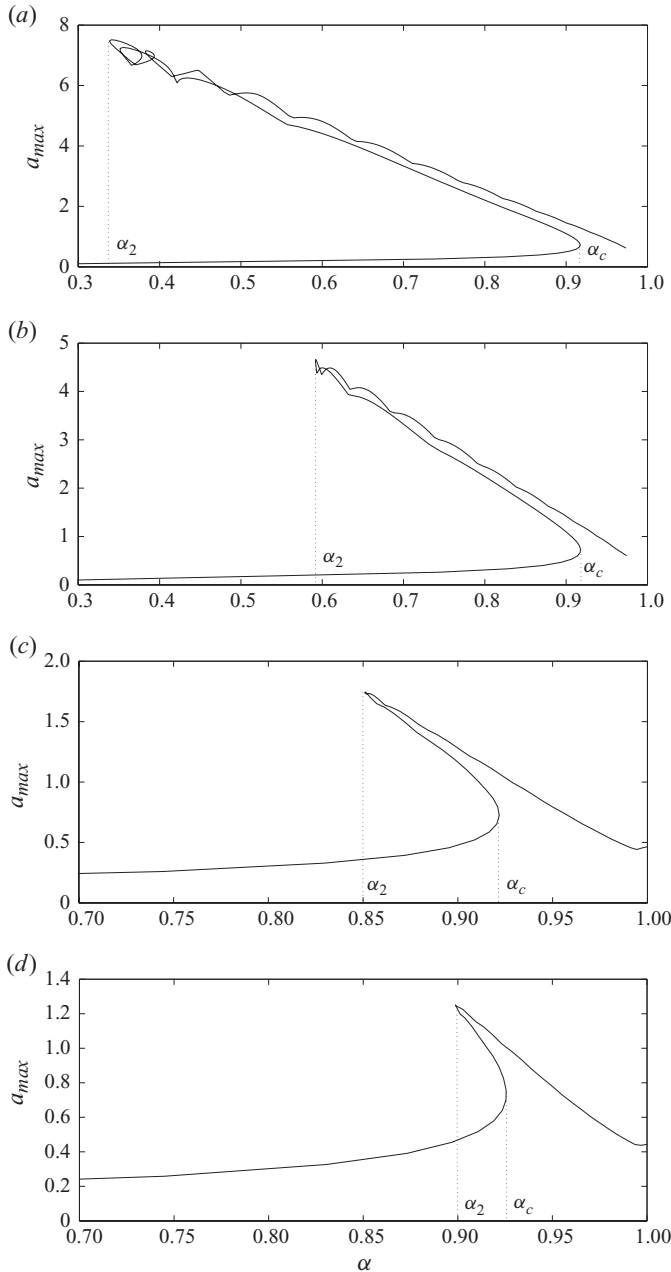
FIGURE 4. Steady-state response diagrams of the maximum depression, $a_{max}$, versus forcing speed $\alpha$, for the excitation amplitude $A = 0.23$ and four different values of the damping parameter $\tilde{v}$. Here $\alpha_c$ and $\alpha_2$ denote the first and second turning points, respectively. (*a*) $\tilde{v} = \tilde{v}_0$; (*b*) $\tilde{v} = 2\tilde{v}_0$; (*c*) $\tilde{v} = 6\tilde{v}_0$; (*d*) $\tilde{v} = 8\tilde{v}_0$; $\tilde{v}_0 = v(4g)^{1/4}(\rho/\tau)^{3/4} = 0.003$ is the value of $\tilde{v}$ pertaining to linear waves (Lamb 1993, §348–349).

to II was observed experimentally for forcing amplitude $\epsilon = 0.43$. The speeds of the profiles displayed in figure 5 were chosen so as to match those of the four experimentally observed profiles in figure 4(*a*–*d*) of Part 1, which illustrate the transition of the response from state I (figure 4*a*) to state II (figure 4*b*–*d*)

| $\tilde{v}$ | $\mu$ | $\alpha_2$ | |
| --- | --- | --- | --- |
| | | Numerical | Analytical |
| $\tilde{v}_0$ | 0.014 | 0.34 | 0.44 |
| $2\tilde{v}_0$ | 0.028 | 0.59 | 0.64 |
| $6\tilde{v}_0$ | 0.083 | 0.85 | 0.89 |
| $8\tilde{v}_0$ | 0.110 | 0.90 | 0.95 |

TABLE 1. Second limit point, $\alpha = \alpha_2$, for the excitation amplitude $A = 0.23$ and four different values of the damping parameter $\tilde{v}$, where $\tilde{v}_0 = v(4g)^{1/4}(\rho/\tau)^{3/4} = 0.003$ is the value of $\tilde{v}$ pertaining to linear waves (Lamb 1993, § 348–349). The analytical estimates for $\alpha_2$ were deduced from the solvability condition (3.12), using $\mu = \tilde{v}/A$; the numerical values of $\alpha_2$ were obtained via continuation in forcing speed $\alpha$ of the small-amplitude steady-state subcritical response.
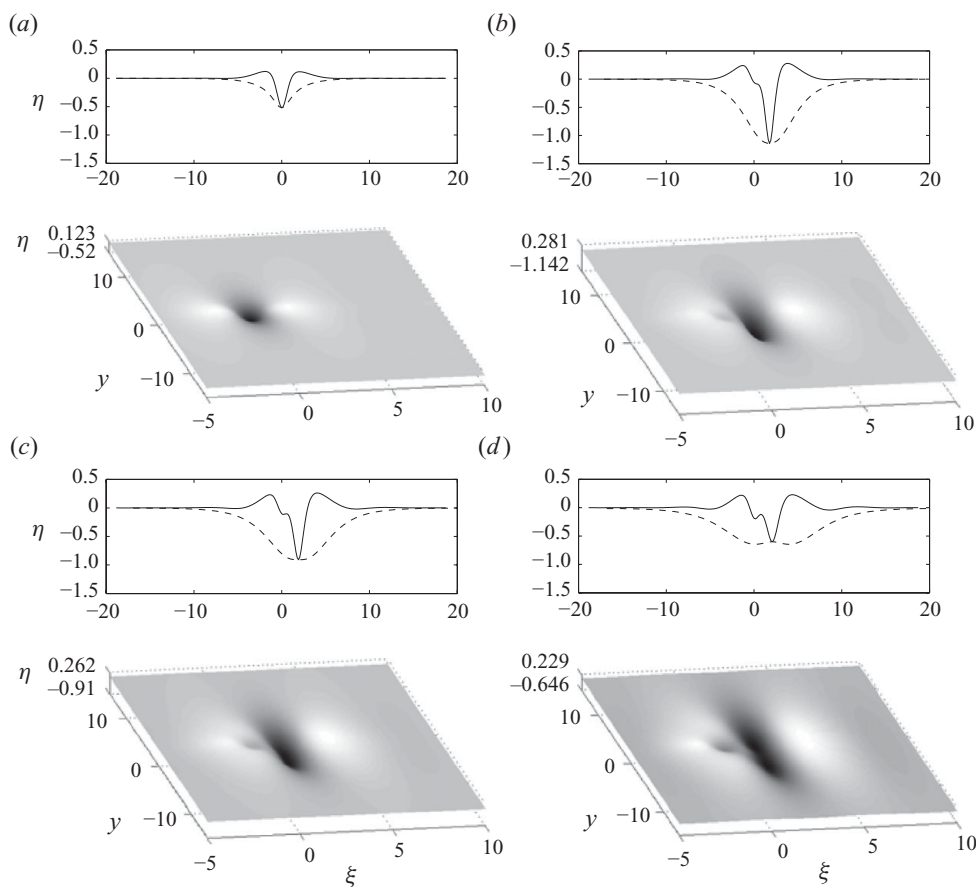


FIGURE 5. Representative steady-state wave profiles at four different forcing speeds $\alpha$ along the response curve shown in figure 4($b$), for the excitation amplitude $A = 0.23$ and damping parameter $\tilde{v} = 2\tilde{v}_0$, where $\tilde{v}_0 = 0.003$. The solid line corresponds to the centreline profile, $\eta(\xi, y = 0)$, and the dashed line corresponds to the transverse profile at the station $\xi$ where the maximum depression is found. ($a$) $\alpha = 0.905$, ($b$) $\alpha = 0.927$, ($c$) $\alpha = 0.948$, ($d$) $\alpha = 0.97$. These speeds match those of the four experimentally observed responses in figure 4 of Part 1.
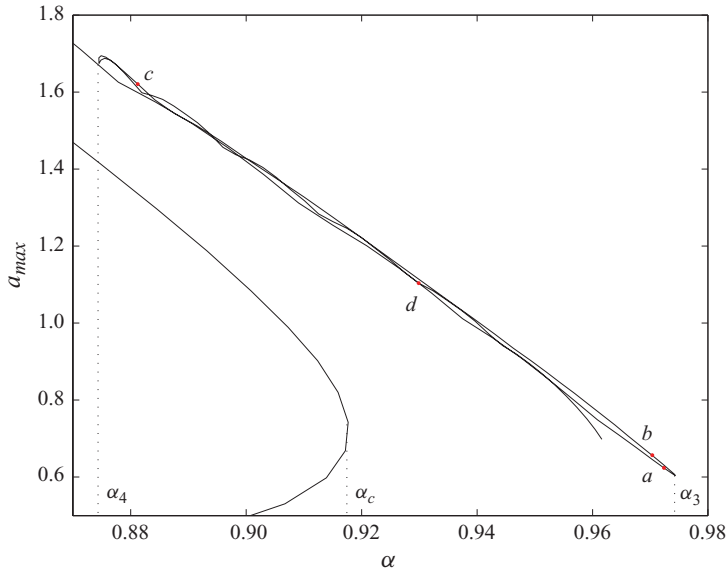
FIGURE 6. Continuation in the forcing speed $\alpha$ past the second limit point $\alpha_2 = 0.59$ (not shown) of the nonlinear solution branch for the excitation amplitude $A = 0.23$ and damping parameter $\tilde{\nu} = 2\tilde{\nu}_0$, where $\tilde{\nu}_0 = 0.003$. Here $a_{max}$ stands for the maximum depression of the response. $\alpha_c = 0.918$ is the first limit point, where the small-amplitude solution branch turns around; $\alpha_3 = 0.974$ and $\alpha_4 = 0.875$ denote the third and fourth turning points, respectively. The wave profiles corresponding to the four points marked $a$–$d$ along the path followed by the nonlinear solution branch are plotted in figure 7.

for $\epsilon = 0.43$. The computed steady-state responses (figure 5) exhibit qualitatively similar behaviour to the observed disturbances. As $\alpha$ is increased past $\alpha_c$, in particular, the lump accompanying state II is shifted further downstream, becoming less steep and more spread out in the spanwise direction, consistent with the observations.

We remark in passing that, for $\tilde{\nu} = \tilde{\nu}_0, 2\tilde{\nu}_0$, where dissipation is relatively low, carrying on the continuation beyond the stage shown in figure $4(a, b)$ reveals a rather intricate behaviour, with the emergence of steady states comprising multiple lumps. Figure 6 shows the detailed path followed by the solution branch for the case $\tilde{\nu} = 2\tilde{\nu}_0$, and figure 7 displays the wave profiles corresponding to four locations along the way, marked $a$–$d$ in figure 6. Note that a third turning point occurs at $\alpha_3 = 0.974$; just prior to reaching there, the response still resembles state II (figure 7$a$), but after turning around at $\alpha_3$, a new steady state emerges featuring two lumps downstream of the pressure distribution (figure 7$b$). Upon further continuation along the same solution branch, the disturbance beneath the applied pressure transforms into a third lump (figure 7$c$), and the entire pattern is shifted downstream (figure 7$d$) after encountering a fourth turning point at $\alpha_4 = 0.875$. This appears to set the stage for the bifurcation of a new state involving more lumps, but we shall not pursue this possibility.

## 4. Transient evolution and comparison with experiment

The steady-state analysis in §3 suggests that the transition from states I to II is associated with the first limit point $\alpha = \alpha_c$; at this critical speed, the response jumps from the small-amplitude state (state I) to the nonlinear state (state II) on the
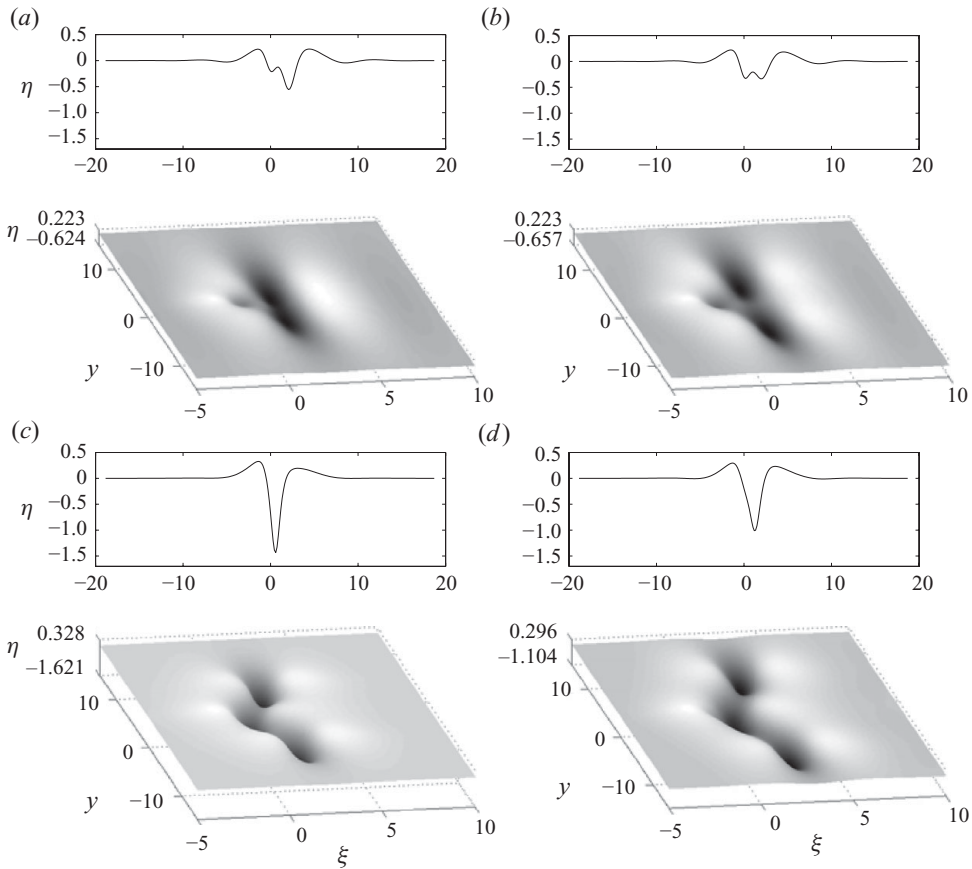
FIGURE 7. Steady-state profiles at the four points marked $a$–$d$ in figure 6 along the path followed by the nonlinear solution branch beyond the second turning point, $\alpha_2$. The one-dimensional plots display the centreline profile $\eta(\xi, y = 0)$. The corresponding forcing speeds are: (a) $\alpha = 0.972$, (b) $\alpha = 0.97$, (c) $\alpha = 0.881$, (d) $\alpha = 0.930$.

solution branch that heads towards $\alpha = 1$ after turning around, due to dissipation, at the second limit point, $\alpha = \alpha_2$ (figure 4). This scenario presumes that state II is stable, which remains to be established. Also, according to the experimental observations, as the forcing speed is increased past $\alpha_c$, there is a second transition, from state II, which is steady, to state III, which is unsteady. To address these issues, we shall turn to numerical investigation of transient responses based on the model equation (2.8).

The numerical technique for solving (2.8) used a spectral approximation in space, combined with a predictor–corrector Euler time stepping (Cho 2010). The results reported here were obtained using the computational domain $(-37.7 < \xi < 37.7, -31.4 < y < 31.4)$ with 512 grid points along $\xi$, 256 grid points along $y$ and time step $\Delta t = 10^{-3}$.

### 4.1. *Stability of state II*

Rather than a formal spectral analysis, the stability of state II was explored by direct numerical integration of (2.8), employing as initial condition the steady solution obtained from continuation and letting numerical error act as the perturbation.
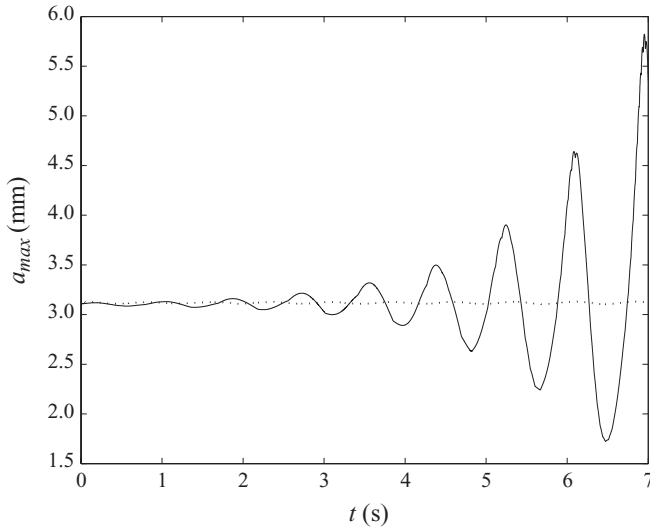
FIGURE 8. Time history of the maximum depression, $a_{max}$ (in mm), as obtained from numerical solution of the model equation (2.8) using as initial condition state II, computed via continuation, for the excitation amplitude $A = 0.23$, speed $\alpha = 0.93$ and two different values of the damping parameter $\tilde{v}$. Lines: —, $\tilde{v} = \tilde{v}_0$; $\cdots$, $\tilde{v} = 2\tilde{v}_0$, where $\tilde{v}_0 = 0.003$ is the value of $\tilde{v}$ pertaining to linear waves.

We first tested the stability of state II for excitation amplitude $A = 0.23$ and dissipation parameter $\tilde{v} = \tilde{v}_0, 2\tilde{v}_0$. Under these conditions, and forcing speed above $\alpha_c$, state II is available in the finite range $\alpha_c < \alpha < \alpha_3$, $\alpha = \alpha_3$ being the third turning point encountered earlier in the course of continuation (figure 6), where $\alpha_3 = 0.975$ for $\tilde{v} = \tilde{v}_0$ and $\alpha_3 = 0.974$ for $\tilde{v} = 2\tilde{v}_0$. Although the steady-state response diagrams corresponding to these two values of $\tilde{v}$ (figure 4 $a, b$) are qualitatively similar, our numerical experiments suggest that state II is unstable for $\tilde{v} = \tilde{v}_0$, but stable for $\tilde{v} = 2\tilde{v}_0$, throughout the speed range $\alpha_c < \alpha < \alpha_3$. Figure 8 illustrates the totally different stability behaviour of state II for $\tilde{v} = \tilde{v}_0$ and $2\tilde{v}_0$ when $\alpha = 0.93$. The oscillatory instability seen for $\tilde{v} = \tilde{v}_0$ is also consistent with the simulations reported in Diorio *et al.* (2009). Our earlier study used the model equation (2.8) with $\tilde{v} = \tilde{v}_0$, and the transient response from rest for $A = 0.21$ and forcing speed $\alpha$ above $\alpha_c$ was found to be periodic in time rather than approaching steady state II. It is now clear that this discrepancy is due to the fact that state II is unstable for the values of the flow parameters used in Diorio *et al.* (2009).

Based on our stability computations, when $\tilde{v} = \tilde{v}_0$, state II turns out to be unstable for $0.08 \leqslant A \leqslant 0.36$, corresponding to $0.86 \leqslant \alpha_c \leqslant 0.98$, which covers the whole range of pressure amplitudes $0.3 \leqslant \epsilon \leqslant 0.69$ used in the experiment (figure 7 in Part 1). Hence, according to our model, $\tilde{v}$ must be greater than $\tilde{v}_0$, the value of $\tilde{v}$ appropriate for linear waves, in order for state II to be stable, as observed experimentally. This seems reasonable, given that the effect of dissipation in steep gravity–capillary solitary waves is considerably stronger than in linear disturbances (Longuet-Higgins 1997), and one would expect the same to be true for lumps as well. However, as the assumed damping term in (2.8) is linear, it is not possible to account for nonlinear effects in viscous dissipation from first principles. In an attempt to allow for this effect in a rough sense, for the remainder of the paper, we shall use $\tilde{v} = 2.4\tilde{v}_0$; this choice implies somewhat stronger viscous dissipation than in weakly nonlinear solitary waves, in
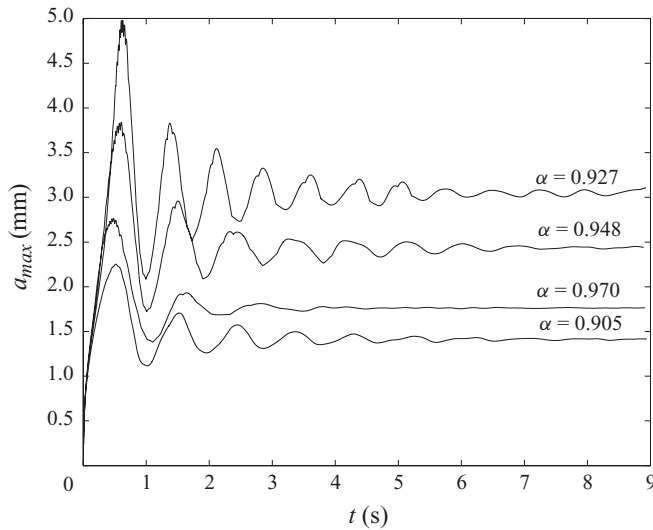
FIGURE 9. Time history of the maximum depression, $a_{max}$ (in mm), associated with transient response starting from rest, for the excitation amplitude $A = 0.23$, damping parameter $\tilde{v} = 2.4\tilde{v}_0$, where $\tilde{v}_0 = 0.003$, and four different forcing speeds $\alpha$. Under these conditions, the response from rest reaches a steady state: state I for $\alpha = 0.905$, but state II for the three higher speeds.

which case $\tilde{v} = 2\tilde{v}_0$ (Longuet-Higgins 1997), and also appears to provide the best overall fit of the model with the observations.

### 4.2. *Transition from state I to state II*

We next studied transient responses from rest. The model equation (2.8) with $\tilde{v} = 2.4\tilde{v}_0$ was integrated numerically turning on the pressure disturbance impulsively at $t = 0$. Several runs were made for excitation amplitude $0.08 \leqslant A \leqslant 0.36$ and speed $0.7 \leqslant \alpha \leqslant 1.03$. As noted above, these conditions cover the entire range of pressure amplitudes and speeds used in the experiment. On the whole, our computations confirm that three distinct subcritical responses, namely states I, II and III, are possible. Here, we focus on states I and II; state III will be discussed in §4.3.

The transient response from rest tends to the small-amplitude steady solution (state I) when the forcing speed $\alpha < \alpha_c$. Upon crossing $\alpha_c$, however, state I is no longer available and is replaced by state II for $\alpha_c < \alpha < \alpha_3$, where $\alpha_3$ denotes the third turning point of the finite-amplitude solution branch computed earlier (figure 6). Based on numerical experiments (see §4.1), for $\tilde{v} = 2.4\tilde{v}_0$ and $0.08 \leqslant A \leqslant 0.36$, state II is stable when $\alpha_c < \alpha < \alpha_3$, and the transient response from rest indeed tends to state II within this range of forcing speeds.

For both states I and II, the approach to steady state features decaying oscillations, with period of roughly 1 s, as illustrated in figure 9 for $A = 0.23$. Similar behaviour was also seen in the experiment, particularly for forcing speeds in the vicinity of $\alpha_c$ (figures 11 and 12 in Part 1). According to our computations, though, the transition from states I to II at $\alpha = \alpha_c$ is sharp, the response invariably tending to one of these two states depending on whether $\alpha < \alpha_c$ or $\alpha > \alpha_c$.

As remarked earlier, $\alpha_c$ is quite sensitive to the excitation amplitude $A$ and so is $\alpha_3$, the upper limit of the speed range $\alpha_c < \alpha < \alpha_3$ in which state II is available. Table 2 lists the values of $\alpha_c$ and $\alpha_3$, obtained from numerical continuation as explained in §3.2, for $\tilde{v} = 2.4\tilde{v}_0$ and the five excitation amplitudes used earlier in the undamped

| $A$ | $\alpha_c$ | $\alpha_3$ |
|------|------|------|
| 0.08 | 0.982 | – |
| 0.16 | 0.948 | 0.989 |
| 0.23 | 0.918 | 0.975 |
| 0.36 | 0.864 | 0.952 |
| 0.42 | 0.839 | 0.942 |

TABLE 2. First ($\alpha = \alpha_c$) and third ($\alpha = \alpha_3$) limit points encountered along the continuation in the forcing speed $\alpha$ of the small-amplitude steady-state subcritical response, for the damping parameter $\tilde{v} = 2.4\tilde{v}_0$, where $\tilde{v}_0 = 0.003$, and five different excitation amplitudes $A$. State II is available in the finite speed range $\alpha_c < \alpha < \alpha_3$. Transition from states I to II occurs at $\alpha_c$ and from states II to III occurs at $\alpha_3$.
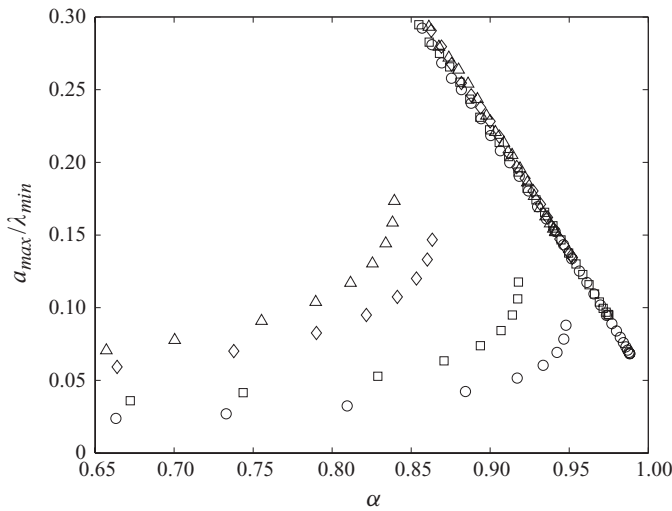


FIGURE 10. Response amplitudes corresponding to states I and II as the forcing speed $\alpha$ is varied, for the damping parameter $\tilde{v} = 2.4\tilde{v}_0$, where $\tilde{v}_0 = 0.003$, and four different excitation amplitudes $A$. Symbols: $\circ$, $A = 0.16$; $\square$, $A = 0.23$; $\diamond$, $A = 0.36$; $\triangle$, $A = 0.42$. As in figure 7 of Part 1, $a_{max}/\lambda_{min}$ stands for the maximum depression of the response normalized with $\lambda_{min} = 17.1$ mm, the gravity–capillary wavelength at $c_{min}$.

($\tilde{v} = 0$) response diagrams in figure 3. While $\alpha_c$ is practically unaffected by the presence of damping, $\alpha_3$ owes its existence to a delicate balance between forcing and damping; for the weakest of the forcings, $A = 0.08$, in particular, no third turning point, $\alpha_3$, is found. In this instance, state II is weakly nonlinear and connects directly with the small-amplitude supercritical response as $\alpha$ is increased past 1.

Figure 10 displays the solution branches associated with states I ($\alpha < \alpha_c$) and II ($\alpha_c < \alpha < \alpha_3$) for four different excitation amplitudes $A$. It is interesting to compare these results with the experimental plots of normalized maximum response depth against forcing speed $\alpha$, shown in figure 7 of Part 1, for four values of the experimental forcing amplitude $\epsilon$. The theoretical forcing amplitudes $A$ have been chosen so that the corresponding values of $\alpha_c$ match roughly the critical speeds at which the response was observed to jump from states I to II, for the four values of $\epsilon$ used in the experiment. It is not surprising, then, that the boundary of state I is well reproduced by the model. More importantly, however, there is also good qualitative agreement
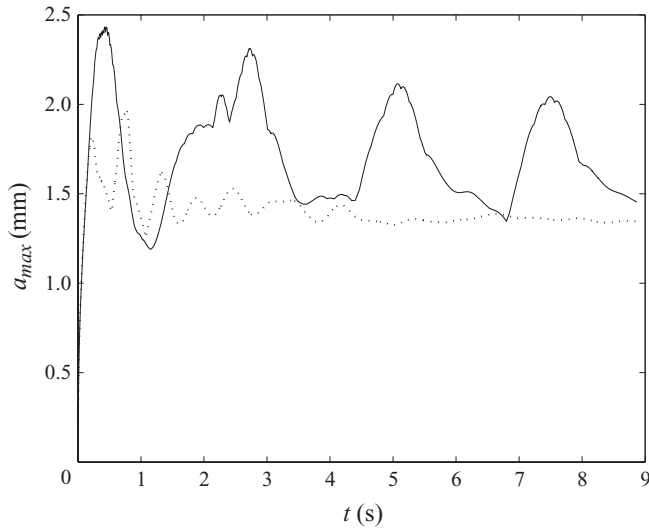
FIGURE 11. Time history of the maximum depression, $a_{max}$ (in mm), associated with transient response starting from rest, for the excitation amplitude $A = 0.23$, damping parameter $\tilde{v} = 2.4\tilde{v}_0$, where $\tilde{v}_0 = 0.003$, and two different forcing speeds $\alpha$. Lines: —, $\alpha = 0.981$; $\cdots$, $\alpha = 1.03$. In the former case, the response reaches a periodic state in time, which corresponds to state III; in the latter, the response reaches the small-amplitude supercritical steady state.

with the experiment with regard to the behaviour of state II. Note, in particular, that the theoretical response curves corresponding to state II in figure 10 essentially follow the same line for all four values of $A$, similar to the experimental data in state II, which collapse on a common line independent of $\epsilon$. For the theoretical responses, this common line is well approximated by the response curve corresponding to free ($A = 0$), inviscid ($\tilde{v} = 0$) lump solutions of the model equation (2.8) (figure 1).

### 4.3. *State III*

The transition from states II to III is associated with the third turning point, $\alpha_3$; state II is not available beyond this speed, and the transient response from rest approaches a periodic state in time, as illustrated in figure 11 for $\alpha = 0.981$ when $A = 0.23$. Note that, for this excitation amplitude, $\alpha_3 = 0.975$, which explains the very different time history of the response in figure 11 compared with that for $\alpha = 0.97$ in figure 9. State III is characterized by periodic shedding of lump-like disturbances downstream of the applied pressure distribution. Figure 12 displays snapshots of the computed response for $\alpha = 0.981$ and $A = 0.23$ at eight times, separated by 0.36 s, which illustrate a full cycle of the shedding process after the periodic state has been reached. At the early stages of the cycle, the pattern has a V shape trailing the pressure excitation (figure 12$a$), but soon the tips of the V transform into lumps (figure 12$b, c$) and the disturbance is reminiscent of the steady states with multiple lumps downstream, computed earlier (figure 7$c, d$); here, however, the lumps detach from the rest of the disturbance and are quickly damped out (figure 12$d$–$g$), thus preparing the way for the cycle to start anew (figure 12$h$). These results are in good qualitative agreement with the experimental observations regarding state III (figures 13 and 14 of Part 1).
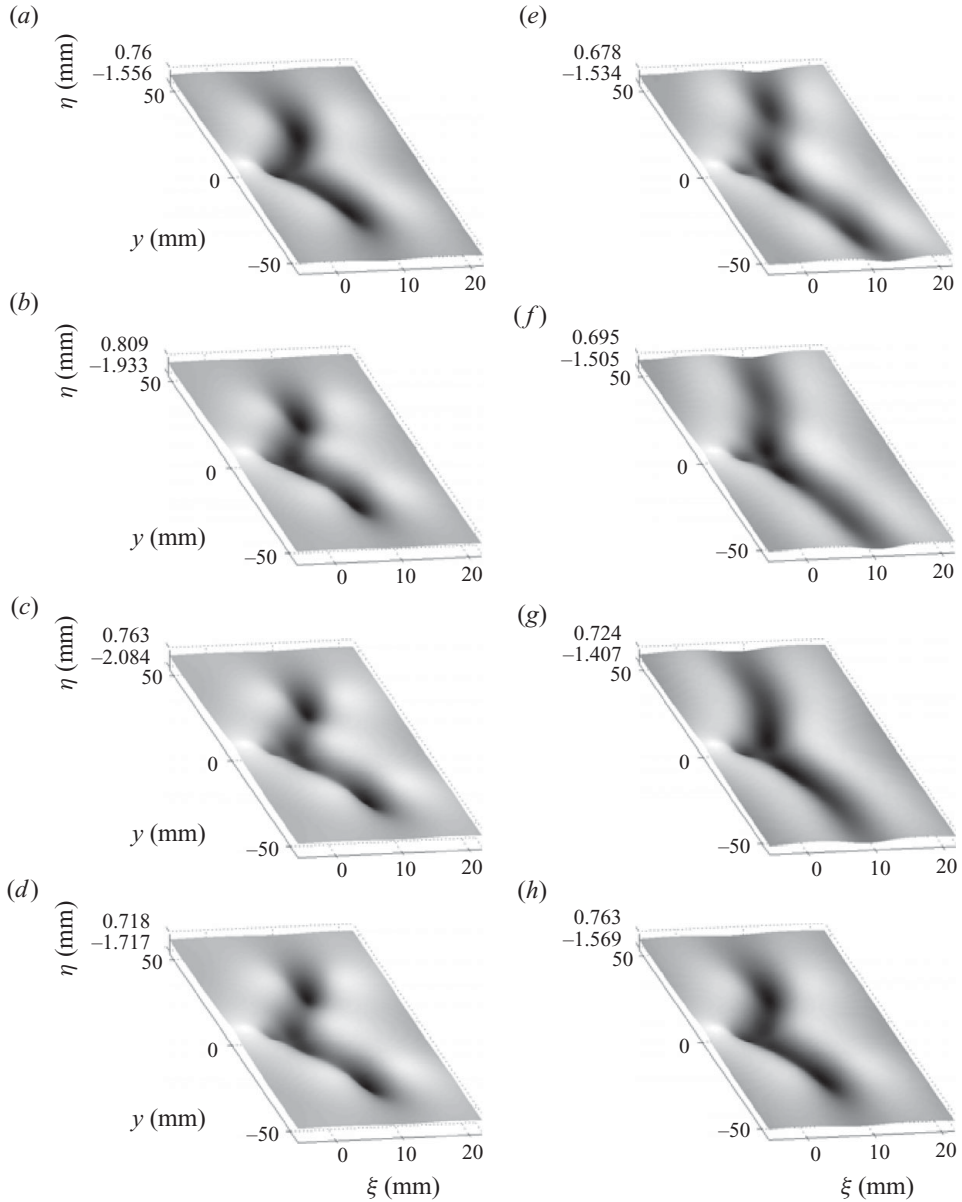
FIGURE 12. Plots at eight different time instants of the induced wave pattern for the excitation amplitude $A = 0.23$, damping parameter $\tilde{v} = 2.4\tilde{v}_0$, where $\tilde{v}_0 = 0.003$, and forcing speed $\alpha = 0.981$. In $(a)$, $t = 4.49$ s and the following plots, $(b–h)$, are separated by 0.36 s. The response corresponds to state III and is characterized by periodic shedding of lumps. The eight snapshots shown cover a full cycle of the shedding process, in qualitative agreement with the experimentally observed state III (figures 13 and 14 of Part 1).

Also, from figure 12$(d–g)$, the decay time of a free lump can be estimated to be about 1 s. Finally, upon increasing $\alpha$ past the critical value $\alpha = 1$, the response from rest returns to a steady state, as illustrated in figure 11 for $\alpha = 1.03$ when $A = 0.23$. This supercritical state is of small amplitude and has a V shape (figure 13), consistent with
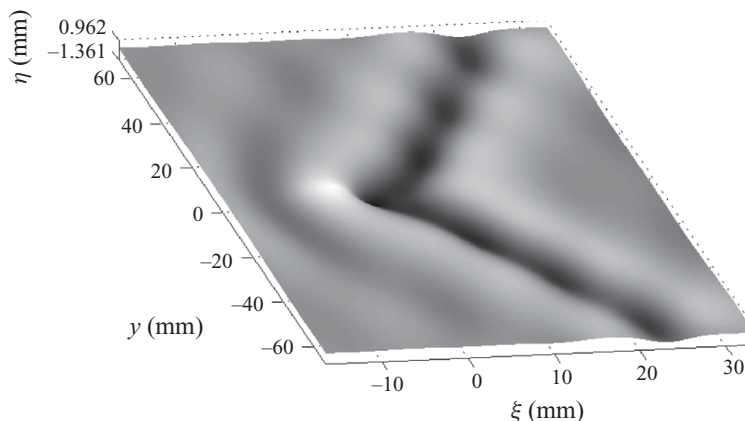
FIGURE 13. Plot of the supercritical steady state reached by transient response from rest for the excitation amplitude $A = 0.23$, damping parameter $\tilde{\nu} = 2.4\tilde{\nu}_0$, where $\tilde{\nu}_0 = 0.003$, and forcing speed $\alpha = 1.03$.

figure 4 (*f*) in Part 1. The transition from state III to the supercritical state has not been studied in detail.

## 5. Discussion

On the basis of the simple model equation analysed here, the precise nature of the forced response near the critical speed $c_{min}$ is determined by a rather delicate balance between nonlinearity, which is controlled by the strength of the applied pressure distribution, and viscous dissipation. Out of the three possible subcritical responses found, states II and III, being nonlinear, are particularly sensitive to this interplay of nonlinear and damping effects. As a result, damping has to exceed a certain threshold in order for state II to be steady as observed experimentally rather than time-periodic, and state III ceases to be available when the pressure amplitude is too weak in comparison to damping.

From a theoretical viewpoint, the prominent role that nonlinearity plays near $c_{min}$ could be somewhat surprising. From either the model equation (2.8) or the full water-wave equations, it is easy to show that, ignoring dissipation, the linear response to localized forcing at speed equal to $c_{min}$ features only a logarithmic singularity, and one might expect that damping would mask nonlinear effects due to this weak resonance. Nonetheless, for forcing speed slightly below $c_{min}$, the response exhibits rich nonlinear behaviour, which must be attributed to the presence of lumps in the subcritical speed range.

In spite of being crude in many respects, the theoretical model proposed here reproduces, at least qualitatively, the main features of the observed responses and seems a viable alternative to fully numerical simulation of the exact governing equations. This type of model could also prove useful in understanding the generation of gravity–capillary lumps in wind-wave experiments (Zhang 1995), as well as in other physical systems where the phase speed features a minimum at non-zero wavenumber (Squire *et al.* 1996).

REFERENCES

AKERS, B. & MILEWSKI, P. A. 2009 A model equation for wavepacket solitary waves arising from capillary–gravity flows. *Stud. Appl. Maths* **122**, 249–274.

AKYLAS, T. R. 1993 Envelope solitons with stationary crests. *Phys. Fluids* A **5**, 789–791.

CHO, Y. 2010 Nonlinear dynamics of three-dimensional solitary waves. PhD thesis, Massachusetts Institute of Technology.

CHO, Y. & AKYLAS, T. R. 2009 Forced waves near resonance at a phase-speed minimum. *Stud. Appl. Maths* **123**, 1–15.

DIORIO, J. D., CHO, Y., DUNCAN, J. H. & AKYLAS, T. R. 2009 Gravity–capillary lumps generated by a moving pressure source. *Phys. Rev. Lett.* **103**, 214502.

DIORIO, J. D., CHO, Y., DUNCAN, J. H. & AKYLAS, T. R. 2011 Resonantly forced gravity–capillary lumps on deep water. Part 1. Experiments. *J. Fluid Mech.* in press.

KAK, S. C. 1970 The discrete Hilbert transform. *Proc. IEEE* **58**, 585–586.

KIM, B. & AKYLAS, T. R. 2005 On gravity–capillary lumps. *J. Fluid Mech.* **540**, 337–351.

LAMB, H. 1993 *Hydrodynamics*, 6th edn. Cambridge University Press.

LONGUET-HIGGINS, M. S. 1993 Capillary–gravity waves of solitary type and envelope solitons on deep water. *J. Fluid Mech.* **252**, 703–711.

LONGUET-HIGGINS, M. S. 1997 Viscous dissipation in steep capillary–gravity waves. *J. Fluid Mech.* **344**, 271–289.

PĂRĂU, E., VANDEN-BROECK, J.-M. & COOKER, M. J. 2005 Nonlinear three-dimensional gravity–capillary solitary waves. *J. Fluid Mech.* **536**, 99–105.

SQUIRE, V. A., HOSKING, R. J., KERR, A. D. & LANGHORNE, P. J. 1996 *Moving Loads on Ice Plates*. Kluwer.

WHITHAM, G. B. 1974 *Linear and Nonlinear Waves*. Wiley-Interscience.

ZHANG, X. 1995 Capillary–gravity and capillary waves generated in a wind-wave tank: observations and theories. *J. Fluid Mech.* **289**, 51–82.